Journal of Zhejiang University-SCIENCE A 2026 27(6):555-568
www.jzus.zju.edu.cn; www.springer.com/journal/11582
E-mail: jzus_a@zju.edu.cn

Research Article
https://doi.org/10.1631/jzus.A2500370

Check for updates

Effect of varying strain rates on the local mechanical properties of aluminum alloy welded joints

Chen LIU[1*], Yansong WANG[1*], Chenmeng WANG[1,2], Hu ZHOU[1], Yuchen YANG[1,3], Bangping GU[1✉], Shibin SUN[1], Long PAN[4], Feilong LIU[5], Guanhua XU[6,7✉], Chuanxiao YANG[1]

[1]*Logistics Engineering College, Shanghai Maritime University, Shanghai 201306, China*
[2]*College of Mechanical Engineering, Donghua University, Shanghai 201620, China*
[3]*School of Mechanical and Power Engineering, East China University of Science and Technology, Shanghai 200237, China*
[4]*School of Mechanical Engineering, Nanjing Institute of Technology, Nanjing 211167, China*
[5]*School of Materials Science and Engineering, Shanghai Jiao Tong University, Shanghai 200240, China*
[6]*State Key Laboratory of Fluid Power and Mechatronic Systems, School of Mechanical Engineering, Zhejiang University, Hangzhou 310058, China*
[7]*Zhejiang Key Laboratory of Additive Manufacturing Technology and Equipment, School of Mechanical Engineering, Zhejiang University, Hangzhou 310058, China*

Abstract: Synchronized stretching in conjunction with digital image correlation (DIC) was employed to obtain stress–strain curves for multiple local regions of welded joints at varying strain rates. The material intrinsic damage model for each region was then fitted using the Ramberg–Osgood equation. As such, we investigated the effects of loads with different strain rates on welded members. The microstructural distribution laws in the local regions were elucidated using scanning electron microscopy (SEM) and optical metallurgical microscopy. Moreover, residual stress concentrations were revealed by employing multi-physics field simulations during the welding process, as well as by using the DIC method for full-field strain measurements. The results demonstrated that tensile specimens with varying strain rates exhibited ductile fracturing and differed in strength and microhardness. The minimum strain-rate tensile strength recorded was 209.727 MPa, with an average microhardness of 72.66 HV0.3. Through simulations, it was further demonstrated that residual stresses and the softening zone cooperate during dynamic loading, resulting in preferential strain concentration. This study elucidates the mechanism by which the strain rate influences the mechanical properties of welded joints and the evolution of local mechanical behavior. It provides theoretical support and technical assurance for safe design and performance enhancement of aluminum alloy welded structures.

Key words: AA5052 aluminum alloy; Digital image correlation (DIC); ABAQUS; Tensile properties

1 Introduction

Aluminum alloys are renowned for their high specific strength, ductility, and fracture toughness (Xing et al., 2025). These properties have led to their widespread use in domains such as ocean engineering, aerospace, and the automotive industry. Overall, they have emerged as pivotal materials for lightweight structural design (Hosseinabadi and Khedmati, 2021; Li et al., 2024; Tian et al., 2024; Koko et al., 2025). The current welding methods for aluminum alloys mainly include cold metal transition (CMT) welding (Sun et al., 2025; Wang et al., 2025), metal inert gas (MIG) welding (Li XY et al., 2025; Yang JH et al., 2025), and tungsten inert gas (TIG) welding (Elamin et al., 2025; Liao et al., 2025). Compared with traditional MIG, TIG, and their ultrasonic-assisted processes (Yang et al., 2024), CMT technology—with its alternating "hot–cold–hot" cycle and precise arc-length control—has been shown to effectively reduce welding heat input. This results in a narrower heat-affected zone (HAZ) and superior original mechanical properties of the welded joint (Wei et al., 2025).

✉ Bangping GU, bpgu@shmtu.edu.cn
Guanhua XU, xuguanhua@zju.edu.cn
* The two authors contributed equally to this work
Bangping GU, https://orcid.org/0000-0001-9558-7120
Guanhua XU, https://orcid.org/0000-0003-4022-7720

Received Oct. 15, 2025; Revision accepted Dec. 11, 2025; Crosschecked May 8, 2026; Online first June 17, 2026

In practical applications, such as offshore engineering, welded joints are often subjected to loads with varying strain rates. Such exposure may arise from a range of external forces, including wave impacts, collisions, and sudden accidents. The strain rate is a pivotal factor in determining the mechanical properties of welded joints; variations in strain rate can induce alterations in the deformation behavior and stress distribution of the material. Consequently, these changes can affect the strength and toughness of the welded joint (Das et al., 2020). Furthermore, it has been demonstrated that residual tensile stresses commonly arise during the welding of aluminum alloys. In conjunction with the softening phenomenon that frequently occurs in the HAZ of welded joints, this has the capacity to degrade the mechanical properties and reliability of welded joints under different strain rates (Sillapasa et al., 2014; Chen et al., 2022a, 2022b; Yang et al., 2023; Ye et al., 2024; Yue et al., 2025). It is therefore essential to comprehensively investigate the impact of strain rate on the mechanical properties of aluminum alloy welded joints. This is necessary to optimize the welding process and enhance the reliability and durability of welded joints (Li ZZ et al., 2022; Xu et al., 2024).

In recent years, scholars have conducted extensive studies of the mechanical properties of aluminum alloys at different strain rates (Lademo et al., 2012; Yan et al., 2016; Çavuşoğlu et al., 2017; Li N et al., 2022). As demonstrated by Getter et al. (2015), ship collision events can induce substantial structural stresses in structures exposed to the sea. The response patterns of these structures exhibit significant variability, and are dependent on the dynamic interactions between the ship and the components of the impacted structure. Therefore, it is imperative to quantify the impact of loads on ships and marine structures and investigate the material failure behavior at varying strain rates. Liu YQ et al. (2024) found that aluminum/steel welded joints exhibit HAZ failure at lower strain rates, and interface failure at higher strain rates. Moreover, Fang et al. (2021) demonstrated that the yield strength and ultimate tensile strength of aluminum alloys—as measured by uniaxial tensile tests at quasi-static, medium, and high strain rates—increase with increasing strain rate. Additionally, the molding characteristics remain similar across different strain rates, with dislocation slip being the plastic deformation mechanism and ductile fracture being the fracturing mechanism. In summary, the failure of welded joints at low strain rates predominantly manifests as either ductile fracturing or steady-state fatigue crack extension. Both of these phenomena are strongly correlated with microscopic defects and localized stress concentrations. Observations of welded joints subjected to elevated strain rates have revealed a tendency toward brittle fracturing, accelerated crack extension, and increased life dispersion. This phenomenon poses a significant challenge to the safety of lightweight structures.

There have been recent advancements in aluminum alloy welded joints, particularly in terms of mechanical characterization and failure mechanisms. However, existing studies continue to exhibit methodological limitations (Yan et al., 2022). For example, current methods are unable to capture localized strain distribution in different areas of the welded joint (welded metal (WM), HAZ, and base metal (BM)). Scholars have also conducted mechanical property testing and analysis of various grades of aluminum alloys over a broad spectrum of strain rates. This has been achieved by employing experimental equipment such as electronic universal testing machines and separate Hopkinson press bars (SHPB), in conjunction with numerical simulations and other approaches (Bragov and Lomunov, 1995; Kumar and Bhattacharya, 2021; Zhao and Kitazono, 2025).

Moreover, digital image correlation (DIC) methods have become an essential research tool for analyzing welded joint deformation (Ren et al., 2025). This technique is predicated on the principle of full-field deformation measurement; by comparing the displacement field distributions across different regions of the component surface, local areas in welded joints with weakened mechanical properties and their spatial distribution characteristics can be identified. Meanwhile, Leitão et al. (2012) used DIC to obtain the local strain field of transverse weld stretching in stir friction welding of aluminum alloy base material. By accounting for local strain data and thickness variations in the specimen, the stress distribution is calculated. Moreover, Hector Jr et al. (2007) measured the yield strength in different regions of aluminum alloy stir friction welding specimens using DIC. This method employs the DIC system to collect local deformation field data, which are then converted into authentic stress–strain relationships via geometric reconstruction algorithms; the parameters are fitted using a nonlinear visco-plastic constitutive model. Moreover, Wu et al. (2020) investigated the local mechanical properties of X80 and

Q235 ring-welded joints, using DIC to conduct tensile tests. The results of these tests allow them to obtain strain distributions for the specimens and identify appropriate stress–strain curves in different regions. In summary, related studies have conducted full-field measurement of the deformation behavior of welded HAZ materials through mechanical experiments on standard tensile specimens and DIC technology; they have also constructed intrinsic relationship models reflecting the associated mechanical responses. However, experimental studies on the mechanisms by which strain rate influences the performance of aluminum alloy welded joints and their local mechanical properties remain insufficient.

This study explores the impact of strain rate on the localized mechanical properties of welded joints. We use DIC technology to capture full-field strain data, integrating this with microhardness testing, fracture morphology analysis, and multiphysics simulations. Moreover, to address the deviation in conversions between real and engineering stress under the complex stress state of the material, a calibration method for correction coefficients leveraging finite element analysis is adopted; this method is used to study the effect of strain rate on the mechanical properties of welded joints using DIC technology. DIC provides insights into the deformation and fracture mechanisms of welded joints under different strain rates. The main objective is to elucidate the failure mechanism of AA5052 aluminum alloy welded joints, and reveal the micro-mechanism by which strain rate influences the tensile properties of aluminum alloys. This study provides theoretical support and technical assurance for the safe design and performance optimization of non-ferrous metal welded structures under complex dynamic loading conditions. As such, reliable safety design and life prediction can be achieved.

2 Methods

2.1 Experimental materials and methods

The experimental specimen was AA5052 aluminum alloy, which is categorized as an Mg-Al alloy. This alloy possesses advantageous properties, including good corrosion resistance, high formability, excellent weldability, and moderate strength. The CMT method (Selvi et al., 2018) was employed for the welding process, and the specimens were prepared as illustrated in Fig. S1 of the electronic supplementary materials (ESM). The AA5052 aluminum alloy and its welding wire were used for the welding process—their chemical compositions are listed in Table S1 of the ESM. The residual stress test using the hole-drilling method, as well as the characterization methods, tensile test, and DIC method, is detailed in the ESM.

2.2 Simulation of aluminum alloy welding

The modeling, meshing, and initialization conditions, as well as the results of the AA5052 aluminum alloy welding simulations, can be found in the ESM. The finite element simulation results indicate that during the welding of AA5052 aluminum alloy, the HAZ experiences significant abnormal grain growth at temperatures of 300–400 °C, resulting in reduced microhardness compared to the BM. Concurrently, thermo-mechanical coupling simulations reveal pronounced residual tensile stress concentrations at the edges of the HAZ. The dual effect of microstructural weakening and stress concentration provides a theoretical foundation for predicting subsequent mechanical property test outcomes. In accordance with the Hall–Petch relationship and the coupled effect of stress concentration, it is reasonable to infer that the HAZ will become the preferred fracture zone under tensile loading. The relevant analysis of results is provided in the ESM.

3 Results

3.1 Microstructural analysis

As shown in Fig. S13 of the ESM, the microstructure of the WM, HAZ, and BM in the CMT welded joint of AA5052 aluminum alloy is clearly delineated. Moreover, we can see that the WM microstructure is predominantly composed of α-Al and Al-Si eutectic, with the molten pool metal within the weld zone undergoing a eutectic reaction; this generates fine Al-Si eutectic at the α-Al boundary once the eutectic temperature is attained during solidification process. The Al-Si eutectic is distributed along the grain boundaries and adheres to the aluminum matrix (Liu S et al., 2024).

A microstructural scanning electron microscopy (SEM) image of the side weld region of a welded joint of AA5052 aluminum alloy is compared with an X-ray diffraction (XRD) diagram of the welded joint in Fig. 1.

The microstructure of the welded joint primarily consists of α-Al, Al_yFe_x, Al-Si, and Al_yMg_x (Kang and Kim, 2015; Liu et al., 2023). The second phase is uniformly dispersed in the matrix α-Al and takes the form of granular, fishbone, and short rods of black color, while the α-Al matrix is grey. Regarding the HAZ, its microstructural characteristics are significantly affected by the welding thermal cycle, leading to partial dissolution and coarsening of the reinforcing phase particles. This sequence of microstructural transformations—particularly the substantial grain coarsening and decline in effective reinforcing phases—directly contributes to the reduction of macroscopic microhardness and strength in the HAZ; this phenomenon is termed "softening." As shown in Fig. S13d of the ESM and Fig. 1b, BM preserves the initial processing condition of AA5052 aluminum alloy. The microstructure of the material exhibits characteristic rolled fibers, with fine and diffuse second-phase particles.

Fig. S14 of the ESM illustrates the microhardness distribution of AA5052 aluminum alloy welded joints in various regions. One can observe that in the HAZ, as the distance from the fusion line increases, the microhardness of the material exhibits a characteristic gradient distribution. The microhardness value is the lowest in the region near the fusion line; it gradually increases as it extends towards the BM, finally reaching a level comparable to that of the BM in the transition zone away from the weld (Yang et al., 2023). Further analysis of the microhardness can be found in the ESM. As shown in Table 1, the microhardness values of the WM and HAZ increased by different magnitudes relative to the unstretched state, with more details again provided in the ESM.

To examine the effect of different strain rates on the tensile plasticity of aluminum alloy welded joints, SEM was used to determine fracture modes and characterize the microfracture features of tensile specimens at different strain rates. As illustrated in Fig. S15 of the ESM, the fracture surface morphology of a rectangular tensile specimen typically exhibits three distinctive regions: the fibrous region, the radiation region, and the shearing-lip region (Long et al., 2023; Li PF et al., 2025). More details on the morphology of macroscopic fractures are delineated in the ESM.

From Fig. 2, we can see that the fracture surface of the original welded joint is characterized by a high density of micro-pores and dimples. This fracture morphology suggests that the joint follows a micro-pore aggregation-type ductile fracturing mechanism (Zhang et al., 2018).

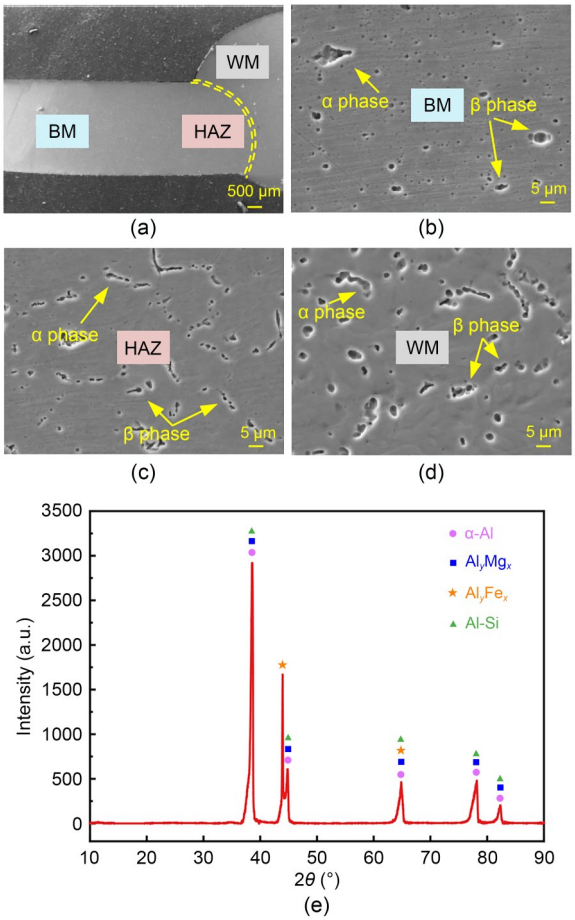

Fig. 1 SEM image of the microstructure of the side of an experimental specimen of AA5052 aluminum alloy: (a) microstructure of the welded joint (30×); (b) microstructure of the BM (3000×); (c) microstructure of the HAZ (3000×); (d) microstructure of the WM (3000×); (e) welded joint XRD diagram

Table 1 Microhardness test on the initial specimen with different parameters relative to the unstretched state

Strain rate (s^{-1})	Microhardness (HV0.3)		
	WM	HAZ	BM
Unstretched	63.78	60.15	70.84
1×10^{-4}	76.59	72.66	70.55
1×10^{-3}	71.34	70.46	69.53
1×10^{-2}	72.51	70.61	68.37
2×10^{-2}	73.93	70.90	68.93

As demonstrated in Figs. 2a, 2d, 2g, and 2j, in the fibrous region, the tensile fracture surface in the HAZ exhibits a larger crater at the slow strain rate of 1×10^{-4} s^{-1} compared to the fast strain rate of 2×10^{-2} s^{-1}. Moreover, the ductility of the aluminum alloy welded joints

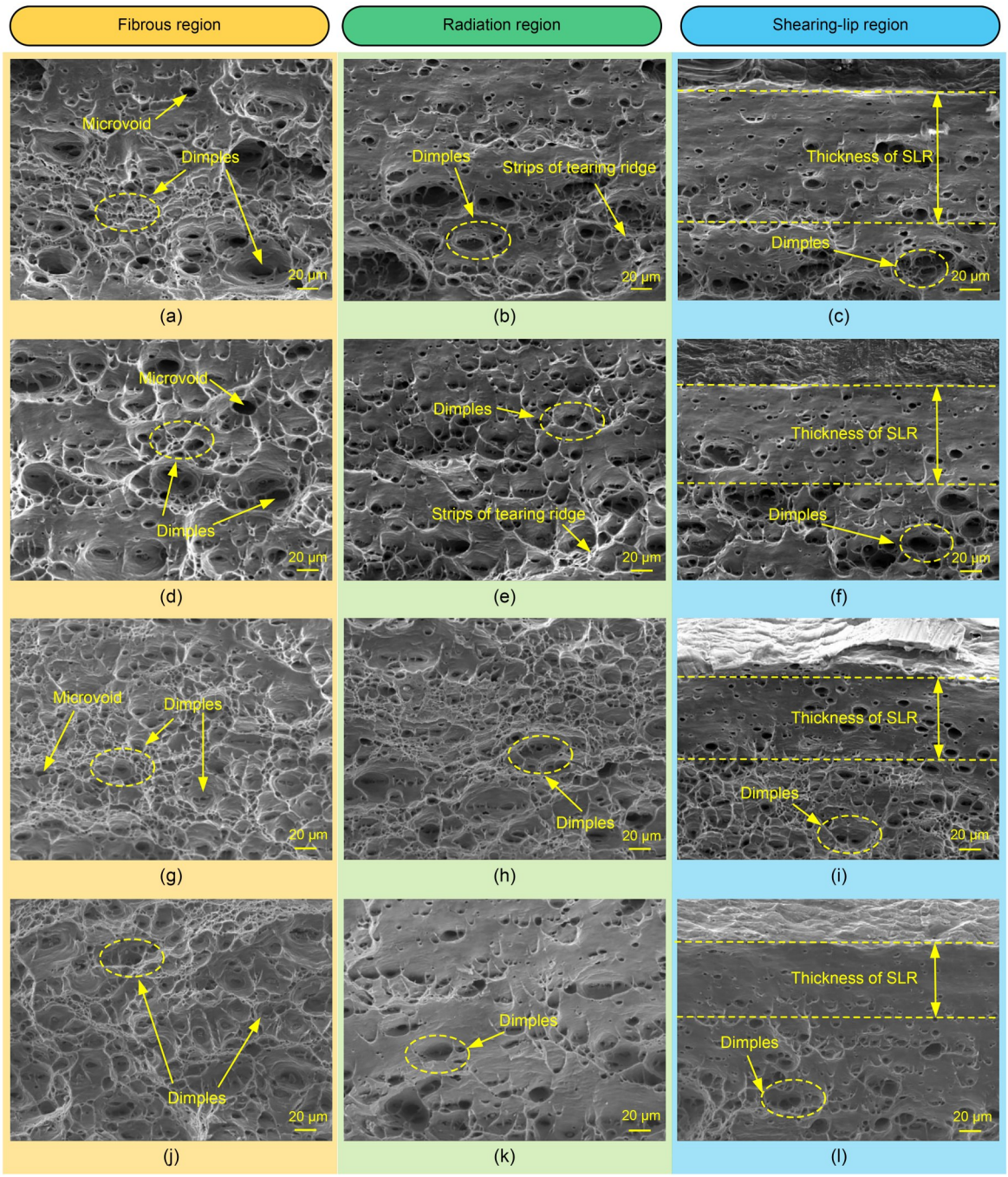

Fig. 2 Microscopic fracture morphology under different conditions in different regions: (a–c) strain rate of 1×10^{-4} s^{-1}; (d–f) strain rate of 1×10^{-3} s^{-1}; (g–i) strain rate of 1×10^{-2} s^{-1}; (j–l) strain rate of 2×10^{-2} s^{-1}

decreases as the strain rate increases from 1×10^{-4} to 2×10^{-2} s^{-1}. Fracturing can initiate from minor surface abrasions or stress concentrations, subsequently propagating across the surface with minimal resistance to shear. Consequently, elongation of the specimen causes a corresponding increase in the diameter and depth of the resulting holes, aligning with the larger dimensions of the dimples. As illustrated in Figs. 2b, 2e, 2h, and 2k, in the radiation region at low strain rates, the aluminum alloy welded joints generally exhibit larger dimples, which is a typical feature of ductile fracture. The greater number of dimples indicates that the material undergoes greater plastic deformation before fracture, as shown in Figs. 2c, 2f, 2i, and 2l. The area of the shearing-lip

region (SLR) decreases in proportion to the increasing strain rate, which is proximal to the fracture surface and exhibits a narrower configuration. Furthermore, an increase in the number of dimples at the fracture site, along with an augmentation in their dimensions, is observed as the strain rate diminishes. This is because at lower strain rates, the material has more time to deform plastically, and dislocation motion is more effective. Consequently, this results in the formation of more micropores and the aggregation of the material into long dimples.

3.2 Influence of strain rate on the PLC effect

The spatial distribution of the Portevin–Le Chatelier (PLC) effect exhibits self-organizing characteristics, as depicted in Fig. S16 of the ESM. To facilitate observation of the PLC effect, the sampling point is located at the fracture. The experimental results show that the stress drop amplitude decreases with an increase in strain rate. Increasing the strain rate causes the solute diffusion rate to reach a dynamic equilibrium with the dislocation motion rate. Furthermore, the waiting time for dislocation in barriers—such as in solute air pockets and forest dislocation—is reduced, thereby facilitating fuller development of the age-hardening effect induced by dynamic strain aging (DSA) (Samanta et al., 2024; Yang HF et al., 2025). This strengthening of the aging mechanism reduces the magnitude of the jagged fluctuations of the macroscopic stress–strain curve. It has therefore been demonstrated that the manifestation of the PLC effect is prone to attenuation.

When the strain rate is excessively high, the interaction time between solute atoms and dislocation is significantly reduced, thereby suppressing the DSA effect and eliminating the PLC phenomenon. Concurrently, the dislocation mobility increases, while the work-hardening capacity declines substantially. The material strength parameters exhibit negative strain-rate sensitivity, which is directly associated with the failure of the dislocation-density proliferation mechanism.

3.3 Local strain distribution in welded joints at different strain rates

The mechanical behavior of the welded joint in different characteristic areas is analyzed in Fig. 3. Across varying strain rates, the stress–strain behavior of each characteristic region of the welded joint differs significantly. Specifically, the integrity of the stress–strain

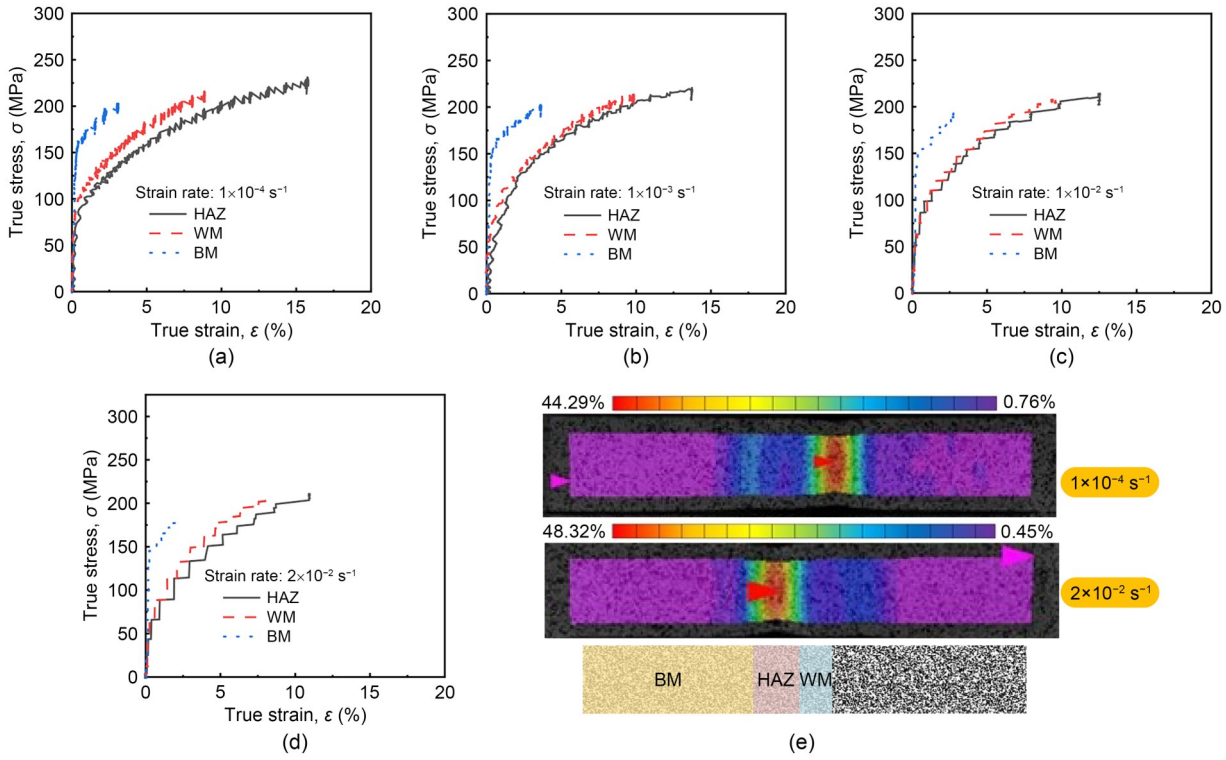

Fig. 3 Stress–strain curves of welded joints at different strain rates: (a) 1×10^{-4} s^{-1}; (b) 1×10^{-3} s^{-1}; (c) 1×10^{-2} s^{-1}; (d) 2×10^{-2} s^{-1}. (e) Welded joint strain distribution map

curve in the HAZ near the fracture is good, whereas the range of responses in the WM and BM is constrained. This is directly related to the high-strength characteristics of the WM and no necking occurred during tensile processes. Following the melt-solidification process in the WM, a significant microstructural reconstruction occurs, resulting in a mixed equiaxial and columnar crystal structure and the precipitation of second-phase particles. This microstructural evolution enhances the local strength but results in a limited range of stress-strain curves in the WM. As the weakest link in the joint, the HAZ microstructure is significantly degraded by the welding thermal cycle. The original deformation microstructure is replaced by a recrystallized microstructure, the reinforcing phase particles coarsen, and the grains grow abnormally. These phenomena together lead to a decrease in microhardness in this region and to the disappearance of the deformation strengthening effect. While the BM is less affected by the welding heat, the microstructure and mechanical properties of the neighboring WM are still altered to a certain degree.

Tensile results for each parameter demonstrate that the material exhibits relatively high strength at low strain rates. This phenomenon can be attributed to the capacity of the material to undergo the DSA process at lower strain rates. At these lower strain rates, the dislocation exhibits reduced mobility, thereby allowing sufficient time for solute atoms to diffuse away from the immediate vicinity of the dislocation and form solute atmospheric clusters. The pinning effect of these solute atoms on the dislocation becomes augmented, leading to impeded dislocation and enhanced material strength. In contrast, at elevated strain rates, the material strain hardens more rapidly and to a greater extent. Here, the DSA effect is relatively weak, and dislocation motion relies primarily on its own stress field to overcome obstacles. This enables the material to continue to deform plastically over a relatively large strain range at high strain rates, which leads to a substantial maximum strain. Concurrently, the strength of the material is diminished at elevated strain rates due to accelerated dislocation motion. This motion makes the solute atoms unable to diffuse adequately, and establishs an effective pinning action. Consequently, the dislocation exhibits relative mobility, leading to a diminished strengthening effect compared to low strain rates.

As the strain rate increases from 1×10^{-4} to 1×10^{-2} s^{-1}, the strength of each region of the joint exhibits a stepwise decrease. When the strain rate increases to 2×10^{-2} s^{-1}, the magnitude of the strength change decreases, indicating a shift in the dynamic response mechanism of the material in this strain rate interval. This strength degradation is primarily attributed to the DSA effect and the strain rate sensitivity (SRS) of the aluminum alloy, with the HAZ exhibiting the most significant decay in strength due to tissue degradation.

3.4 Influence of different strain rates on the local properties of welded joints

To construct the intrinsic relationship model, the experimental curves were characterized using the aforementioned data-fitting method. Key material parameters, including tensile strength (σ_t), hardening index (n), and strength coefficient (K), were obtained. Young's modulus (E) was determined by fitting the initial linear segment of the stress–strain curve. The yield strength σ_s was determined from the stress–strain curve using the 0.2% offset criterion. K and n were solved for by an iterative optimization algorithm based on the modified Holloman formula. The tensile strength σ_t was extracted at the peak point of the stress–strain curve. σ_t^* represents the ultimate tensile strength. EXT stands for extension. The results of the parameter calculations under different strain-rate conditions are summarized in Table 2.

Fig. 4 presents the fitted stress–strain curves for tensile specimens under four distinct process parameters, which demonstrate close alignment with the DIC curves. As shown in Fig. 4 and Fig. S19 of the ESM and Table 2, as the strain rate diminishes, both σ_t and the average σ_s in the BM, HAZ, and WM become augmented. In comparison to the condition with a strain rate of 2×10^{-2} s^{-1}, the most significant effect is achieved under the parameters of 1×10^{-4} s^{-1}, as shown in Figs. S19a and S19c of the ESM. The WM improvement is the most notable, with an improvement rate of 31.54%. Overall the order is WM>HAZ>BM. As for the improvement effect of σ_t in each region under various parameters, these results are shown in Figs. S19b and S19d of the ESM. Here, the slowest strain rate also leads to the best improvement effect, with BM showing the most significant enhancement; this corresponds to an improvement rate of 8.46%, and the order is BM> HAZ>WM.

A comparison of the strength enhancement effect in the local area of the welded joints reveals that the

Table 2 Effect of different process parameters on the intrinsic properties of the welded joints

Strain rate (s^{-1})	Area	σ_s (MPa)	n	K (MPa)	σ_t^* (MPa)	σ_t (MPa)	σ_s/σ_t
1×10^{-4}	BM	161.957	0.172	364.038	268.935	226.409	0.715
	HAZ	103.917	0.287	399.956	279.536	209.727	0.495
	WM	104.453	0.296	433.549	302.319	224.927	0.464
1×10^{-3}	BM	156.579	0.162	343.664	255.919	217.563	0.720
	HAZ	101.297	0.266	382.842	269.086	206.165	0.491
	WM	88.604	0.316	437.202	303.684	221.325	0.400
1×10^{-2}	BM	153.200	0.159	334.477	249.648	212.814	0.720
	HAZ	97.786	0.276	380.775	266.799	202.386	0.483
	WM	80.290	0.320	437.297	303.911	220.569	0.364
2×10^{-2}	BM	149.310	0.161	329.119	245.206	208.743	0.715
	HAZ	87.037	0.259	369.830	260.618	201.084	0.433
	WM	79.405	0.295	419.887	292.999	218.029	0.364

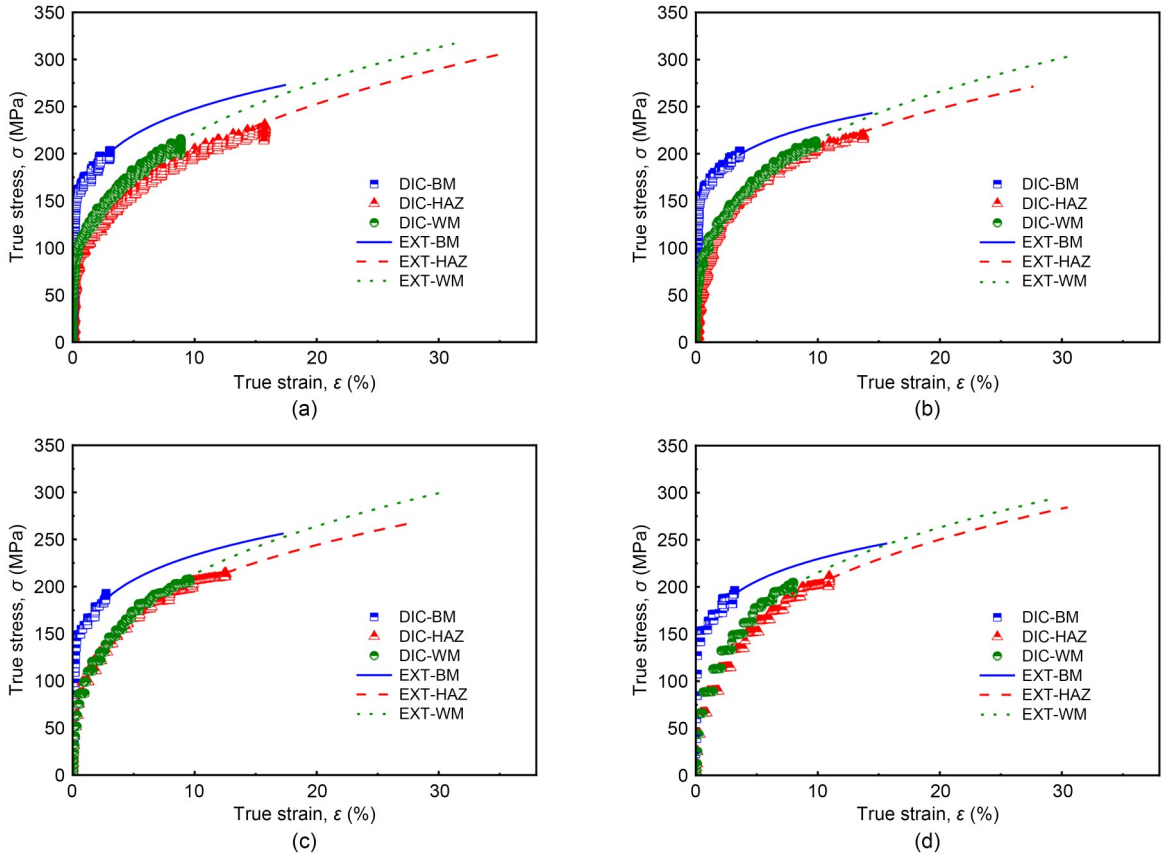

Fig. 4 Fitted stress–strain curves with different parameters: (a) strain rate of 1×10^{-4} s^{-1}; (b) strain rate of 1×10^{-3} s^{-1}; (c) strain rate of 1×10^{-2} s^{-1}; (d) strain rate of 2×10^{-2} s^{-1}

σ_s enhancement effect is more pronounced than the tensile strength enhancement effect. The n, a pivotal parameter in the material constitutive relationship, quantitatively describes the average evolution law of material strain hardening during the stage of homogeneous plastic deformation. Additionally, it reflects the capacity of a material to resist sustained plastic deformation. From a physical perspective, the n value indicates the efficiency of dislocation structural evolution during material deformation. A higher n value signifies accelerated dislocation accumulation, more comprehensive grain orientation adjustment, and a more pronounced

hardening effect. Work hardening results from increased dislocation density and its interaction with barriers—such as grain boundaries—leading to a continuous increase in deformation resistance. Materials with high n values can undergo uniform deformation over extended periods, thereby enhancing their formation limits and energy absorption capacity.

The experimental data in Fig. S21a of the ESM show that n increases gradually from BM to WM across different strain-rate conditions. According to dynamic strain-aging theory, variation in n is influenced by the interaction between solute atoms and dislocation. At low strain rates, sufficient time is provided for solute atoms to diffuse and interact with the dislocation, thereby enhancing the work-hardening capacity of the material. However, when the strain rate is excessively high, the diffusion of solute atoms is unable to keep pace with the movement of the dislocation; this leads to a weakening of the dynamic strain-aging effect and a subsequent decrease in the n value.

From Fig. S21a of the ESM we can observe a directional increase in the strength coefficient K, going from the BM to the WM location. The lowest value is observed at BM, while the peak occurs at WM. According to the Hollomon equation, K is associated with the dislocation density of the material and the solute atom concentration. At low strain rates, the dislocation density is increased by the strong interaction between solute atoms and dislocation, and thus the K value increases. However, when the strain rate is excessively high, the dislocation density is reduced by insufficient solute atom diffusion and relatively free dislocation movement, thereby diminishing the K value.

The yield-to-tensile strength ratio is indicative of the uniform deformation capacity of the material. As illustrated in Fig. S21b of the ESM, at low strain rates, the interaction between solute atoms and dislocation is relatively strong, and the material exhibits good uniform deformation capability. However, at elevated strain rates, the capacity of the material to undergo uniform deformation is diminished because of inadequate solute atom diffusion and localized deformation.

Figs. S13 and S21 of the ESM demonstrate that the distinct microstructures in the BM, HAZ, and WM regions give rise to different dislocation motion mechanisms and DSA effects across varying strain rates, thereby resulting in different strain-rate sensitivities. The elevated grain-boundary density in the WM region has been shown to more effectively impede dislocation motion, accordingly providing more time for solute-atom diffusion and amplifying the DSA effect (Samanta et al., 2024). When strain rates become too high, solute atom diffusion cannot keep up with the dislocation motion; as a result, the dynamic strain aging effect weakens, leading to decreases in n and K.

3.5 Influence of different strain rates on the work hardening rate

The strain hardening characteristics of the material were characterized by calculating the instantaneous strain hardening rate parameter, using the true stress–strain curve in conjunction with the K–M model (Kocks and Mecking, 2003). The results of this are presented in Fig. S22 of the ESM.

Among the WM, HAZ, and BM, the strain rate exerts the most significant influence on the strain-hardening rate in the HAZ. Moreover, the WM and BM regions of the AA5052 aluminum alloy welded joint exhibit greater hardening capacity than the HAZ, at both of the tested strain rates. Slower strain rates yield superior strain hardening capability.

4 Discussion

As shown in the finite element simulation results of Section 2, the welding process introduces significant residual tensile stress to the HAZ. This stress field shows spatial coupling with the HAZ microstructure evolution discussed in Section 3.1. This dual mechanism of "microstructural softening–stress concentration" provides a key basis for understanding the fracture behavior of the joint under quasi-static tensile loading. Under tensile loading, the external load superimposes on the inherent residual tensile stress in the HAZ, causing the local equivalent stress in this area to reach the material's yield and fracture-critical values more quickly. All tensile specimens fracture preferentially in the HAZ. Furthermore, the strain concentration observed in the HAZ through DIC provides experimental confirmation that this region represents a weak link in mechanical properties. Consequently, residual stresses and microstructural softening synergistically dominate the fracture path selection, ultimately determining the overall mechanical performance and reliability of the welded joint. As demonstrated in the preceding analysis, a substantial correlation exists between the residual stress

distribution in the HAZ and the fracture mechanism for aluminum alloy welded joints. In Sections 2 and 3.4, we discussed how the fracture position in the tensile experiment is highly consistent with the high-stress zone of the HAZ as predicted by the simulation. An analysis of the fracture surface using SEM reveals that the fracture initiation point is in the transition zone between the HAZ and weld interface. This area exhibits typical ductile fracture characteristics. The finite element simulation of thermal-force coupling indicates that during welding, the HAZ undergoes a nonuniform thermal cycle; this results in an obvious residual tensile stress field in this area. The disparity in cooling rate during the solidification stage of the molten pool generates a plastic strain gradient, leading to the formation of stress concentration zones on both sides of the WM. Such a stress distribution is closely related to the microstructural evolution of the material. The thermal cycling effect causes the HAZ to undergo grain coarsening and dissolution during the strengthening phase, leading to local softening. The simulation results demonstrate that the cumulative equivalent plastic strain in this area significantly increases compared to the BM, thereby confirming the synergistic effect of microstructural weakening and stress concentration.

In addition, using DIC technology to monitor the strain distribution during the tensile process enables confirmation of an abnormal strain concentration at the elastic stage of the HAZ. When the applied load is superimposed with the residual tensile stress, this area reaches the critical fracture strain threshold more quickly. This experimental phenomenon can be explained by the dual mechanism of "microstructural softening–stress concentration." The residual tensile stress has been shown to reduce the effective local bearing section while accelerating fracturing by promoting micropore nucleation. This in turn causes preferential expansion of the fracture path along the HAZ.

The reduction of the SRS coefficient even shows a negative phenomenon (Samanta et al., 2024). Based on the classical DSA theoretical framework (Nowak et al., 2024), this phenomenon arises from the dynamic interaction between solute atoms and dislocation, and is typically prominent at lower strain rates. Under high strain rate conditions, the material exhibits a significant strain rate strengthening effect. At this time, the influence of DSA is relatively limited, resulting in a continuously increasing stress level with larger strain rates.

As demonstrated in Fig. 5 (Zhou, 2023), at the point where the strain rate reaches its maximum, dislocation-initiated dynamic precipitation occurs, prompting the rearrangement of the saturated solute atoms that have initially precipitated. This process leads to a decline in the concentration of solute atoms. Currently, the number of dynamic precipitated phases is limited, and the dilution effect of the solute atoms reduces the stress increment; this is primarily because plastic deformation introduces a substantial number of dislocations. The dislocation lines and the strain fields around them are highly effective nucleation sites for the precipitating phase, thereby reducing the barrier to nucleation (Pieranski et al., 2023; Chen et al., 2025). The solute atoms (predominantly magnesium) subsequently diffuse to the potential nucleation sites, forming new precipitation phases.

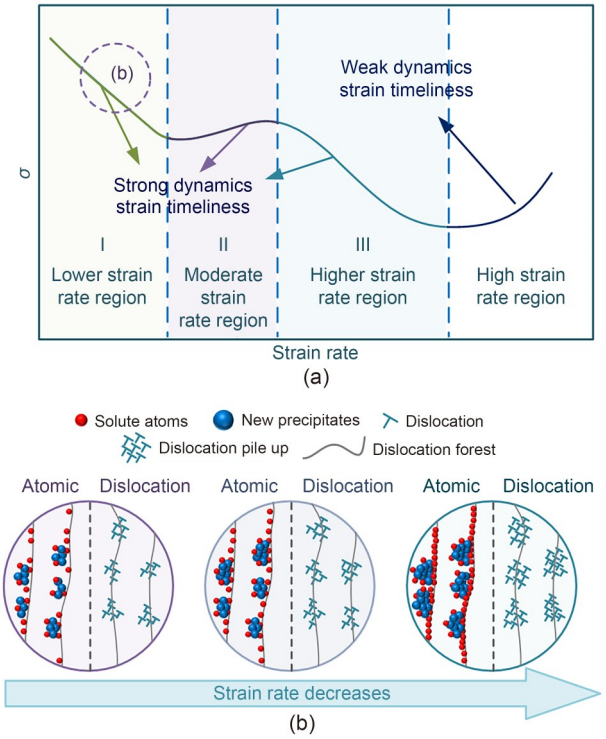

Fig. 5 Schematic diagram of the micro-mechanism of the variation of stress with strain rate: (a) strain rate curve; (b) mechanistic diagram

As the strain rate decreases to a specific threshold, the DSA effect gradually intensifies and becomes the dominant factor, thereby exhibiting a negative sensitivity to strain rate. As the strain rate decreases into the medium range, the stress–strain curve again shows an upward trend. Further reduction of the strain rate into

the low-speed region leads to the re-emergence of negative SRS in the material.

When the strain rate is reduced, the concentration of solute atoms surrounding the Lin dislocation reaches saturation, which induces the precipitation of a second phase around the dislocation—this phenomenon is known as a dynamic precipitation process. Despite the low strain rate, the continuous deformation process will still generate and accumulate dislocation. It has been demonstrated that lower strain rates can permit dislocation to interact for longer, for instance, through entanglement and the formation of cellular structures. These complex dislocation structures offer a broader array of potential nucleation sites. It has also been established that during dynamic precipitation, the newly formed precipitated phase acts as an additional obstacle to dislocation motion. This phase can effectively reduce the average free path for dislocation movement. Furthermore, it can increase the energy required to activate the sliding system, thereby triggering the redistribution of saturated solute atoms on the forest dislocation. As a result, the concentration of solute atoms in the vicinity of the dislocation decreases, attenuating the dynamic strain-aging effect as the strain rate declines; consequently, the stress levels are reduced. Therefore in this region, the stress increases with strain rate.

When the strain rate is reduced, the continuous increase in the volume fraction of the precipitated phase becomes the dominant factor. The amount of precipitated phase then continues to increase, resulting in a smaller distance between the precipitated phases. Certain studies have demonstrated that the probability of the dislocation-encircling phenomenon (Orowan type) depends on the proximity between second-phase particles (Samanta et al., 2024). Concurrently, the reduction in spacing increases the stress required for dislocation to bypass second-phase particles, thereby enhancing their tensile strength (Guo et al., 2025). Moreover, the stress increment generated by the precipitation strengthening effect exceeds the stress loss caused by the redistribution of solute atoms. The Orowan mechanism intensifies if the quantity of dynamically precipitated phases is sufficient to increase the stress more than the reduction caused by solute atom redistribution; consequently, the total stress rises again as the strain rate decreases. Linn dislocation readily impedes the motion of mobile dislocation in aluminum alloys. The combined effect of solute atom diffusion, aggregation, and precipitation further intensifies the pinning of stacking faults. At the same time, solute atoms gradually diffuse, and as the strain rate decreases, the dwelling time of dislocation at obstacles increases. This intensifies the DSA effect and exacerbates dislocation pinning. Meanwhile, the accumulation of solute atoms reduces interatomic distances, enhancing dislocation stacking and making slip systems more resistant to activation. This results in higher stress values at lower strain rates than at higher strain rates.

5 Conclusions

The present study explores the effect of strain rate on the macroscopic and microscopic mechanisms governing the tensile properties of an aluminum alloy. Specifically, we examine the impact of varying strain rate parameters on the microstructural and mechanical properties of AA5052 aluminum alloy welded joints.

A combination of welding simulations and experiments is employed to reveal the development of residual tensile stresses and stress concentrations in the HAZ during welding. These stresses are attributed to the uneven heating and cooling of the material. Concurrently, microstructural softening occurs in this region and interacts with the stress, collectively influencing the mechanical behavior of the welded joint.

A microstructural examination reveals that the weld zone features refined grains and a uniform microstructure, which is predominantly comprised of equiaxed α-Al grains and eutectic Al-Si phases. The HAZ exhibits softening due to recrystallization and has the lowest microhardness. Moreover, the hardness test results indicate that the BM exhibits the highest microhardness (70.84 HV0.3), followed by the WM (63.78 HV0.3), and finally the HAZ (60.15 HV0.3). Through tensile testing, an enhancement in the microhardness of the specimens is observed, which is attributed to the increase in dislocation density.

The tensile fracture of the initial welded joint manifest due to the aggregation of many micropores and dimples, indicating that the aluminum alloy joint specimen undergoes micropore aggregation-type fracturing. We also find that tensile specimens at different strain rates exhibit ductile fractures, and that the fracture morphology is strongly affected by the strain rate; as the strain rate decreases, the dimple size at the fracture

surface increases. This is because at a lower strain rate, the material has more time to undergo plastic deformation—the dislocation movement is thus more thorough, forming a greater amount of micropores and aggregating longer dimples.

Compared to the scenario at a strain rate of 1×10^{-4} s^{-1}, the strength of each area of the welded joint at 1×10^{-3} s^{-1} is lower. This is due to dynamic strain aging and strain-rate effects in the aluminum alloy, which lead to reductions in σ_s and tensile strength across the welded joint. When the strain rate is 1×10^{-2} s^{-1}, the strength of each area of the joint continues to decrease; the influence of the increasing strain rate on the strength is relatively strong. However, when the strain rate is 2×10^{-2} s^{-1}, the strength of each area of the welded joint does not differ significantly from the previous three groups. Among the three regions, the strain rate has the greatest influence on the work hardening rate in the HAZ.

The experimental results show that as the strain rate decreases, the average ultimate strength and average σ_s in the WM, HAZ, and BM all improve. At a strain rate of 1×10^{-4} s^{-1}, the average σ_s of the WM, HAZ, and BM of the specimens are increased by 25.0, 16.9, and 12.6 MPa, respectively, compared with those at 2×10^{-2} s^{-1}; meanwhile, the average tensile strength values are increased by 6.9, 8.6, and 17.7 MPa, respectively, compared with those at 2×10^{-2} s^{-1}. Furthermore, as the strain rate decreases, the improvement in the tensile properties of the welded joint becomes greater. The experimental findings demonstrate that within the quasi-static strain rate range (1×10^{-4}–2×10^{-2} s^{-1}), decreasing the strain rate enhances the strength and hardening capacity of the AA5052 joints; this is because of the DSA effect. However, further investigation is necessary to elucidate the specific mechanisms behind this sensitivity to varying strain rates.

Acknowledgments

This work is supported by the National Natural Science Foundation of China for Young Scholars (Nos. 52105466 and 51805477) and the National Natural Science Foundation of China (No. 52305028). The authors thank the Eceshi (www. eceshi. com) for the SEM test.

Author contributions

Bangping GU designed the research. Hu ZHOU, Chenmeng WANG, Yuchen YANG, Long PAN, and Feilong LIU processed the corresponding data. Chen LIU and Yansong WANG drafted the paper. Chuanxiao YANG and Shibin SUN helped organize the paper. Bangping GU and Guanhua XU revised and edited the final version.

Conflict of interest

Chen LIU, Yansong WANG, Chenmeng WANG, Hu Zhou, Yuchen YANG, Bangping GU, Shibin SUN, Long PAN, Feilong LIU, Guanhua XU, and Chuanxiao YANG declare that they have no conflict of interest.

Declaration on the use of generative AI tools

During the preparation of this work, the authors used ChatGPT, Deepl, and Grammarly to improve language and readability. After using this tool, the authors reviewed and edited the content as needed and take full responsibility for the content of the publication.

Data availability

The data that support the findings of this study are available from the corresponding author upon reasonable request.

References

Bragov AM, Lomunov AK, 1995. Methodological aspects of studying dynamic material properties using the Kolsky method. *International Journal of Impact Engineering*, 16(2): 321-330. https://doi.org/10.1016/0734-743X(95)93939-G

Çavuşoğlu O, Leacock AG, Gürün H, et al., 2017. Strain-rate-dependent tensile characteristics of AA2139-T351 aluminum alloy. *Materiali in Tehnologije*, 51(2):333-348. https://doi.org/10.17222/mit.2016.009

Chen GX, Hu CY, Hou TP, et al., 2025. Probing the interplay among elevated-temperature mechanical properties, microstructural evolution, and dynamic strain aging in reduced activation ferritic/martensitic steels. *Journal of Materials Research and Technology*, 35:3593-3604. https://doi.org/10.1016/j.jmrt.2025.01.229

Chen Y, Chen WS, Hao H, et al., 2022a. Damage evaluation of a welded beam–column joint with surface imperfections subjected to impact loads. *Engineering Structures*, 261: 114276. https://doi.org/10.1016/j.engstruct.2022.114276

Chen Y, Chen WS, Hao H, et al., 2022b. Impact behavior of beam-column joint with geometric imperfections at weld root. *Engineering Structures*, 266:114611. https://doi.org/10.1016/j.engstruct.2022.114611

Das A, Beaumont R, Butterworth I, et al., 2020. High rate and temperature-dependent tensile characterisation with modelling for gap-bridged remote laser welded (RLW) joint using automotive AA5182 alloy. *International Journal of Impact Engineering*, 144:103672. https://doi.org/10.1016/j.ijimpeng.2020.103672

Elamin NY, Elamin MR, Alhussain H, et al., 2025. Influence of Cu and Ni addition on metallurgical, mechanical, and corrosion behavior of TIG welded Al-Mg-Si alloy. *International*

Journal of Pressure Vessels and Piping, 216:105533. https://doi.org/10.1016/j.ijpvp.2025.105533

Fang JX, Zhu ZY, Zhang XQ, et al., 2021. Tensile deformation and fracture behavior of AA5052 aluminum alloy under different strain rates. *Journal of Materials Engineering and Performance*, 30(12):9403-9411. https://doi.org/10.1007/s11665-021-06112-5

Getter DJ, Kantrales GC, Consolazio GR, et al., 2015. Strain rate sensitive steel constitutive models for finite element analysis of vessel-structure impacts. *Marine Structures*, 44:171-202. https://doi.org/10.1016/j.marstruc.2015.09.001

Guo HF, Wang YS, Wang MY, et al., 2025. Microstructure, wear, and corrosion resistance of HVOF WC24-$Cr_3C_2$57-NiCr19 coating. *Tribology International*, 211:110806. https://doi.org/10.1016/j.triboint.2025.110806

Hector Jr LG, Chen YL, Agarwal S, et al., 2007. Friction stir processed AA5182-O and AA6111-T4 aluminum alloys. Part 2: tensile properties and strain field evolution. *Journal of Materials Engineering and Performance*, 16(4):404-417. https://doi.org/10.1007/s11665-007-9060-0

Hosseinabadi OF, Khedmati MR, 2021. A review on ultimate strength of aluminium structural elements and systems for marine applications. *Ocean Engineering*, 232:109153. https://doi.org/10.1016/j.oceaneng.2021.109153

Kang M, Kim C, 2015. Joining Al 5052 alloy to aluminized steel sheet using cold metal transfer process. *Materials & Design*, 81:95-103. https://doi.org/10.1016/j.matdes.2015.05.035

Kocks UF, Mecking H, 2003. Physics and phenomenology of strain hardening: the FCC case. *Progress in Materials Science*, 48(3):171-273. https://doi.org/10.1016/S0079-6425(02)00003-8

Koko A, Salim D, Leung N, et al., 2025. Exploring short crack behaviour and fracture transition in 5052 aluminium alloy. *Results in Engineering*, 26:105303. https://doi.org/10.1016/j.rineng.2025.105303

Kumar I, Bhattacharya A, 2021. Strain rate effect on tensile behavior of AA6061-T6 friction stir welds. *CIRP Journal of Manufacturing Science and Technology*, 35:323-335. https://doi.org/10.1016/j.cirpj.2021.06.023

Lademo OG, Engler O, Benallal A, et al., 2012. Effect of strain rate and dynamic strain ageing on work-hardening for aluminium alloy AA5182-O. *International Journal of Materials Research*, 103(8):1035-1041. https://doi.org/10.3139/146.110741

Leitão C, Galvão I, Leal RM, et al., 2012. Determination of local constitutive properties of aluminium friction stir welds using digital image correlation. *Materials & Design*, 33:69-74. https://doi.org/10.1016/j.matdes.2011.07.009

Li BB, He PC, Wang JF, et al., 2024. Mechanical characteristic and stress-strain modelling of friction stir welded 6061-T6 aluminium alloy butt joints. *Thin-Walled Structures*, 198: 111645. https://doi.org/10.1016/j.tws.2024.111645

Li N, He JY, Zhou YH, et al., 2022. Strain rate effects on the mechanical responses in Mo-alloyed CoCrNi medium entropy alloys. *Materials Science and Engineering: A*, 856: 143944. https://doi.org/10.1016/j.msea.2022.143944

Li PF, Huang H, Du WZ, et al., 2025. Mechanical properties and fracture mechanism of high-strength FGH4097 superalloys prepared by hot oscillatory pressing. *Journal of Materials Research and Technology*, 35:3008-3020. https://doi.org/10.1016/j.jmrt.2025.01.197

Li XY, Sun GR, Ren BQ, et al., 2025. Microstructure and mechanical properties of 7075 aluminum alloy welded joints fabricated by MIG welding with 7085-Sc welding wire. *Materials Science and Engineering: A*, 944:148969. https://doi.org/10.1016/j.msea.2025.148969

Li ZZ, Yan HG, Chen JH, et al., 2022. Enhancing damping capacity and mechanical properties of Al-Mg alloy by high strain rate hot rolling and subsequent cold rolling. *Journal of Alloys and Compounds*, 908:164677. https://doi.org/10.1016/j.jallcom.2022.164677

Liao HQ, Zhao XH, Liu Y, et al., 2025. Investigation of optimizing mechanical properties of 441 stainless steel welded joints via the synchronous ultrasound radiation assisted TIG welding. *Journal of Materials Research and Technology*, 37:929-937. https://doi.org/10.1016/j.jmrt.2025.05.215

Liu HD, Pu J, Wu MF, et al., 2023. Research on the microstructure and properties of Al alloy/steel CMT welding-brazing joints with Al–Si flux-cored welding wires. *Coatings*, 13(9): 1590. https://doi.org/10.3390/coatings13091590

Liu S, Liu ZQ, Wang HJ, et al., 2024. Study on microstructure and mechanical properties of 5052 aluminum alloy MIG welded joint for high-speed train. *Materials Research Express*, 11(8):086507. https://doi.org/10.1088/2053-1591/ad6b01

Liu YQ, Li YX, Zhu ZT, et al., 2024. Effect of strain rate on tensile characteristics and failure behavior of Al/steel welded joint producing by a laser-MIG composite heating source. *Engineering Failure Analysis*, 164:108689. https://doi.org/10.1016/j.engfailanal.2024.108689

Long SL, Yi YL, Gui Q, et al., 2023. A novel model to predict microvoid evolution in tensile necking using macroscopic deformation behavior. *Journal of Materials Research and Technology*, 25:2040-2048. https://doi.org/10.1016/j.jmrt.2023.06.072

Nowak C, Zhou XW, Sills RB, 2024. Validating continuum theory for Cottrell atmosphere solute drag by molecular dynamics simulations. *Journal of the Mechanics and Physics of Solids*, 183:105514. https://doi.org/10.1016/j.jmps.2023.105514

Pieranski P, Zeghal M, Godinho MH, et al., 2023. Topological metadefects: tangles of dislocations. *Physical Review Letters*, 131(12):128101. https://doi.org/10.1103/PhysRevLett.131.128101

Ren SC, Morgeneyer TF, Rousselier G, et al., 2025. Re-straining induced triggering of the Portevin-Le Chatelier effect in recrystallised 2198 T3 and T8 aluminium alloy: experimental observations and FE simulations for smooth and notched samples. *International Journal of Solids and Structures*, 323:113636.

https://doi.org/10.1016/j.ijsolstr.2025.113636

Samanta S, Sahoo JR, Mishra S, 2024. Effect of dynamic strain ageing on flow stress and critical strain for jerky flow in Al-Mg alloys. *International Journal of Plasticity*, 180:104053. https://doi.org/10.1016/j.ijplas.2024.104053

Selvi S, Vishvaksenan A, Rajasekar E, 2018. Cold metal transfer (CMT) technology - an overview. *Defence Technology*, 14(1):28-44. https://doi.org/10.1016/j.dt.2017.08.002

Sillapasa K, Surapunt S, Miyashita Y, et al., 2014. Tensile and fatigue behavior of SZ, HAZ and BM in friction stir welded joint of rolled 6N01 aluminum alloy plate. *International Journal of Fatigue*, 63:162-170. https://doi.org/10.1016/j.ijfatigue.2014.01.021

Sun GR, Du WB, Li WL, et al., 2025. Synergistic strengthening of arc-directed energy deposited aluminum composites via nanoparticles and metastable phase precipitation. *Additive Manufacturing Frontiers*, 4(4):200252. https://doi.org/10.1016/j.amf.2025.200252

Tian HY, Cui ZY, Zhang B, et al., 2024. Atmospheric corrosion and mechanical property degradation of 2524-T3 aluminum alloy in marine environments. *Corrosion Science*, 239:112398. https://doi.org/10.1016/j.corsci.2024.112398

Wang W, Wu DT, Yin HD, et al., 2025. Research on additive manufacturing and properties of Ni-Al-Cr medium-entropy alloy. *Materials Today Communications*, 46:112912. https://doi.org/10.1016/j.mtcomm.2025.112912

Wei W, Sun YJ, Zhang C, et al., 2025. Effect of CMT and MIG welding on microstructure and mechanical properties of Al-Zn-Mg-Cu-Er-Zr alloy. *Materials*, 18(20):4688. https://doi.org/10.3390/ma18204688

Wu X, Shuai J, Xu K, et al., 2020. Determination of local true stress-strain response of X80 and Q235 girth-welded joints based on digital image correlation and numerical simulation. *International Journal of Pressure Vessels and Piping*, 188:104232. https://doi.org/10.1016/j.ijpvp.2020.104232

Xing BY, Chen JC, Yan ZM, et al., 2025. Influence of heat treatment on cracks and mechanical properties of self-piercing riveted joint in aluminum alloy. *Chinese Journal of Engineering Design*, 32(3):359-366 (in Chinese). https://doi.org/10.3785/j.issn.1006-754X.2025.04.177

Xu WF, Wang C, Lu HJ, et al., 2024. Effect of strain rates on stress corrosion sensitivity of 7085-T7452 thick-plate friction stir welding joint. *Materials Characterization*, 218:114554. https://doi.org/10.1016/j.matchar.2024.114554

Yan R, Xin HH, Yang F, et al., 2022. A method for determining the constitutive model of the heat-affected zone using digital image correlation. *Construction and Building Materials*, 342:127981. https://doi.org/10.1016/j.conbuildmat.2022.127981

Yan SL, Yang H, Li HW, et al., 2016. Variation of strain rate sensitivity of an aluminum alloy in a wide strain rate range: mechanism analysis and modeling. *Journal of Alloys and Compounds*, 688:776-786. https://doi.org/10.1016/j.jallcom.2016.07.077

Yang HF, Pei JF, Shi MT, et al., 2025. Plastic deformation mechanism of high manganese steel via laser laminated object manufacturing. *Journal of Materials Processing Technology*, 342:118935. https://doi.org/10.1016/j.jmatprotec.2025.118935

Yang JH, Ji PF, Wu LY, et al., 2025. MIG welding microstructure, residual stress and mechanical properties of powder metallurgy 7A52 aluminum alloys. *Transactions of Nonferrous Metals Society of China*, 35(8):2500-2520. https://doi.org/10.1016/S1003-6326(25)66829-4

Yang SH, Yang XY, Lu X, et al., 2023. Strength calculation and microstructure characterization of HAZ softening area in 6082-T6 aluminum alloy CMT welded joints. *Materials Today Communications*, 37:107077. https://doi.org/10.1016/j.mtcomm.2023.107077

Yang Z, Wang BC, Sun SJ, et al., 2024. Design and analysis of flexible intelligent ultrasonic welding workstation. *Chinese Journal of Engineering Design*, 31(3):377-382 (in Chinese). https://doi.org/10.3785/j.issn.1006-754X.2024.24.107

Ye Z, Zhu HY, Wang SF, et al., 2024. Fabricate high-strength 7075 aluminum alloy joint through double pulse MIG welding process. *Journal of Manufacturing Processes*, 125:512-522. https://doi.org/10.1016/j.jmapro.2024.07.066

Yue KJ, Miao QY, Ma GY, et al., 2025. Crack-free pulsed laser welding of 7075 aluminum alloy: microstructure, crack prediction, and mechanical properties. *Journal of Manufacturing Processes*, 146:159-171. https://doi.org/10.1016/j.jmapro.2025.04.094

Zhang WL, Chen XF, Zhuo BC, et al., 2018. Effect of strain rate and temperature on dynamic mechanical behavior and microstructure evolution of ultra-high strength aluminum alloy. *Materials Science and Engineering: A*, 730:336-344. https://doi.org/10.1016/j.msea.2018.06.018

Zhao RS, Kitazono K, 2025. Strain rate sensitivity of additively manufactured Al-Mg-Sc alloy lattice structures at room temperature. *Materials Today Communications*, 49:113728. https://doi.org/10.1016/j.mtcomm.2025.113728

Zhou P, 2023. Evolution of Microstructure and Properties of High Strength Aluminum Alloy During Deformation-Step Fast Aging. PhD Thesis, Wuhan University of Technology, Wuhan, China (in Chinese). https://doi.org/10.27381/d.cnki.gwlgu.2023.000115

Electronic supplementary materials

Sections S1–S3, Tables S1–S3, Figs. S1–S22